INEXPENSIVE VERIFICATION VIA ELECTROMECHANICAL IMPEDANCE FOR ADDITIVELY MANUFACTURED PARTS

Scott M. Strutner *1, Charles Tenney *2,3, Pablo A. Tarazaga 2, Christopher B. Williams 3,
Andrew M. Kwas 1

* Authors of equal contribution

- 1 Northrop Grumman Corporation, Herndon, VA, 20171
- 2 Vibrations, Adaptive Structures, and Testing Laboratory
 3 Design, Research, and Education for Additive Manufacturing Systems Laboratory
 Department of Mechanical Engineering, Virginia Tech, Blacksburg, VA, 24061

ABSTRACT

Currently, verifying additively manufactured (AM) parts requires time consuming and expensive nondestructive evaluation (NDE) processes such as computed tomography (CT) x-ray scanning. While such methods provide details on flaw type and location, they require significant cost and time. Often, in production environments, significant value is gained by rapidly screening part specimens for flaws at all. Cost-effective per-specimen testing for production runs of AM parts is important for their use to be economically justified. In this work, Northrop Grumman Corporation and Virginia Tech explored impedance-based testing as a means to evaluate AM titanium specimens. Specimens with and without manually-designed flaws were fabricated through a metalbased AM process and evaluated using the impedance-based technique. CT scans confirmed that the intended flaws in the experimental specimens were present. Impedance-based examination also showed the presence of unintended defects. After machining away the unintended defective regions, the flaw-containing defective specimen had a clearly different impedance 'signature' than non-flawed baseline specimens. Additional analysis confirmed that the impedance test method required cheaper capital equipment and required less technician time to examine test results. Taken together, this means that the impedance-based this method can reduce the total cost of utilizing AM for metal part manufacturing.

1. INTRODUCTION

Increased complexity offered by additive manufacturing (AM) processes provides novel challenges to existing non-destructive evaluation (NDE) techniques. Assembly reduction through combination of components, use of a wide range of materials, incorporation of meso- and microscale structures, and use of post-processing techniques such as hot isostatic pressing (HIP) are just a few AM capabilities that challenge existing methods of inspection. Beyond these, NDE techniques used in industry must also fulfill the requirements for speed, accuracy, and expense in order to be useful for standard in-line inspection [1]. Ultimately, the key screening question for many AM parts is "Does this specimen have a mechanical flaws present large enough to pose a threat to structural integrity?" and the inability of existing NDE techniques to cheaply and quickly address this question hinders the wider adoption of AM processes for end-use production. In this study, impedance-based electromechanical inspection (EMI) and computed tomography (CT) x-ray scanning are used to examine titanium specimens and detect the presence of defects. Results

of both types of inspection are presented, illustrating how defects are detected in both cases. Finally, a cost analysis of each method is presented.

1.1 Computed Tomography X-ray Inspection

Though NDE techniques exist with greater accuracy at the surface, such as white light interferometry, and there are other techniques capable of sub-surface sensing, such as eddy-current and ultrasonic testing, CT x-ray scanning provides the highest level of detail throughout the volume of complex parts [2]. The use of CT for manufacturing quality assurance involves projecting a cone-shaped, x-ray beam through a specimen and onto an x-ray sensitive panel. The specimen is rotated while the panel measures the attenuation of the beam many times. Attenuation depends on the composition and thickness of material in the beam's path. Reconstruction software applied to the collected measurements generates a 3D voxel representation of the distribution of attenuating material throughout the specimen [3]. The maximum resolution achievable is determined by the focus spot size of the x-ray emitter, the pitch of the detector's pixels, and the amount of magnification produced by the relative distances between the emitter, specimen, and detector. For thin specimens with overall dimensions in millimeters, this can result in a resolution of tens of nanometers [4]. For larger specimens on the order of tens of centimeters, magnification is reduced and the beam power required to penetrate the specimen limits the emitter focus size, resulting in a resolution on the order of tens to hundreds of microns [5].

Slices of the 3D representation can then be extracted, producing images where the brightness of each pixel represents relative x-ray attenuation. The presence of sufficiently sized voids, porosity, and contamination/inclusion produce dark spots on the image. Analysis of these images, whether done digitally or by a technician, allows determination of the precise size, type, and location of defects in a specimen.

The increasing demand for inspections of larger and more geometrically complex metallic parts has led to the construction of CT machines with higher-voltage emitters, higher resolution sensors, large and expensive synchrotron or linear accelerator x-ray sources, and more-sophisticated reconstruction algorithms. However, these advanced machines are more expensive, starting at \$100,000 and extending up to more than \$600,000. In addition, the setup of each scan, as well as the interpretation of the reconstructed image requires hours of a technician's time, despite the increasing automation of the data analysis process.

1.2 Impedance-based Non-destructive Evaluation

To address the need for more cost- and time-effective NDE techniques for AM parts, the team has explored an impedance-based NDE technique called electromechanical impedance (EMI). Impedance-based NDE methods examine the dynamic vibrational response of a specimen, comparing it to an established 'baseline' response and interpreting deviations as indications of defects in the specimen. To this purpose, a lead zirconate titanate (PZT) piezoelectric element bonded to the specimen is used as a collocated actuator and sensor: as voltage signals applied to the element produce mechanical vibration, and those vibrations create reverse potentials, the mechanical response of the structure is inferred through measurement of the electrical impedance of the element, hence the EMI name. This technique relies on the understanding that manufacturing defects in a specimen produce changes to the mass, stiffness, and damping that can be inferred from changes in the frequency and magnitude of the resonances in its dynamic response.

This technique is rooted in the field of structural health monitoring (SHM) where the 'baseline' is measured for a specimen in its as-built state. For structures such as bridges or aircraft [6], the measurements might be repeated after an earthquake or as part of routine inspection to determine if damage has occurred, and if so, determine the type and location of the damage. This information can aid in predicting the remaining useful life of the structure and inform the decision to perform condition-based maintenance. The development of piezoelectric elements as actuators [7], and investigations into the use of electrical impedance of bonded elements to infer structural characteristics [8, 9], would lead to the development of high-frequency interrogation for the detection of small, local defects [10].

In this work, a variation of the SHM technique is used in which a group of specimens are compared to each other, rather than comparing a specimen to itself over time. The response of each specimen is obtained by measuring the electrical impedance of a bonded PZT element, which acts as a collocated actuator and sensor. Due to the electromechanical coupling of PZT, the electrical characteristics of the bonded PZT reveals the mechanical characteristics of the attached specimen. The baseline measurement is thus established by characterizing a group of 'control' specimens that are taken to be defect-free (via current acceptance and NDE testing methods), and the response of potentially-defective specimens is compared to that baseline. This technique has been previously used to examine polymer-based AM specimens, in which voids of 8 mm³ were successfully detected post-fabrication [11]. Previous investigations of this technique studied its use for in-situ monitoring of polymer specimens during fabrication [12], the effect of void size and proximity of voids to the piezoelectric element [13], and the effect of how the piezoelectric element is attached to the specimen [14].

The wide bandwidth excitation made possible by this technique, on the order of 10-500 kHz [10], differentiates it from impact-based resonant approaches which have limited bandwidth to <25 kHz. This means that minimum detectable defect size through EMI is limited by process variability, rather than excitation limitations. It is also relatively inexpensive, both in the cost of the sensors and measurement equipment. Proposals exist for simplified, single-purpose measurement devices at a fraction of the price of the multi-function lab equipment used in this work [15].

2. TEST SPECIMEN FABRICATION AND INSTRUMENTATION

2.1 Design of Test Specimens

Two versions of the test part were designed: one control (defect-free) design, and one 'defective' design including features that simulate cracks and internal voids. In Figure 1A, an isometric view of the defect-free control design is shown, while Figure 1B contains a cross-section of the defective design to display the designed internal and external defects. Overall, the test specimen geometry qualitatively mimics a heat exchanger cross-section. It also incorporates features intended to produce several CT imaging artifacts such as curved surfaces to induce scattering, abrupt changes in thickness to induce streaking and beam hardening, and a large number of fine features in the center of the part where imaging is more difficult.

For the defective version, defect features were included at two main locations: 1) crack-like features were inserted around the outer circumference of the part to provide an easily-imaged

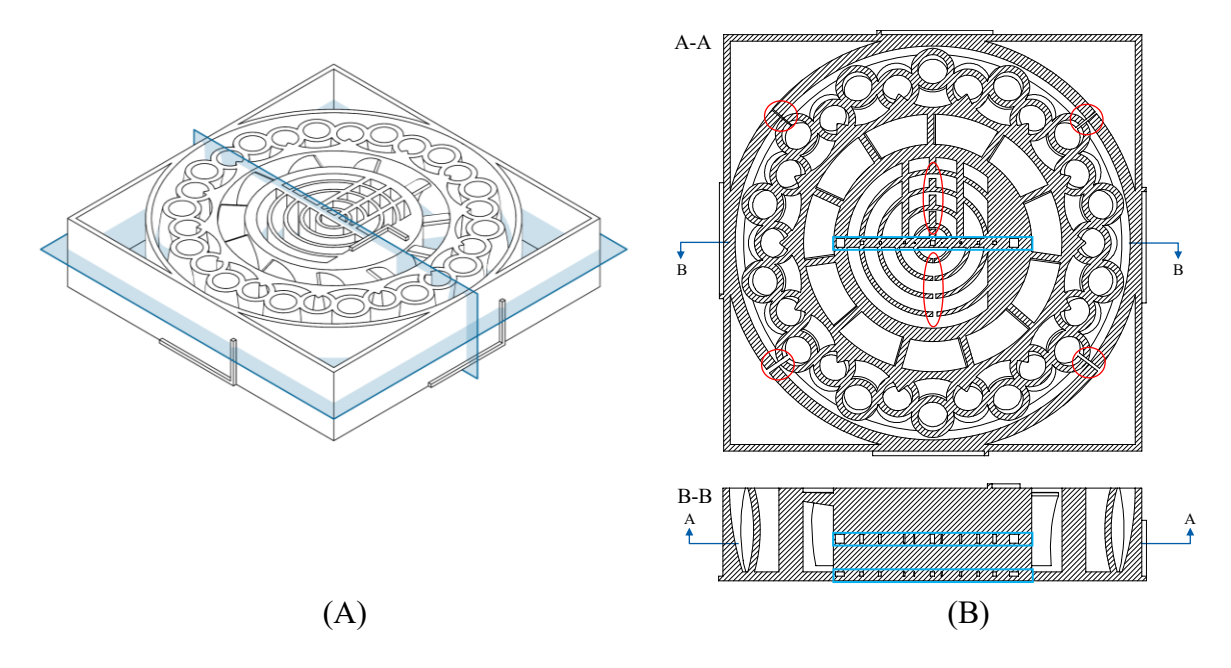


Figure 1. (A) The defect-free control part with two reference planes. (B) Cut-aways of the defective design of the part for each of the reference planes, showing internal 'voids' filled with un-fused powder (blue rectangle) as well as 'cracks' in circular features (red ovals).

reference, and 2) void features were included in the center to challenge the capabilities of the CT scanner. At both locations, the features were included over a range of nominal sizes: crack-like features were sized at 0.3, 0.5, 0.8, and 1.0 mm thickness, and void features were elongated squares of 0.2, 0.4, 0.6, 0.8, 1.0, and 2.0 mm side length, but consistent 2.0 mm depth. An additional void feature was included in one of the curved fins.

The overall dimensions of the part and the sizes of the defect features were limited by the AM machine available. Each specimen fit in a $100 \times 100 \times 20$ mm bounding box, allowing the two control and one defective specimens to lie flat within the footprint of the 200 mm side-length square print bed. Arranging the specimens in the powder bed this way reduced the total print time and cost, and was intended to avoid variability produced by different lots of powder, or inhomogeneity through the height of the print bed.

Titanium was used for these parts as it sees extensive use in aerospace due to its material properties, but remains a very expensive material. The desire to reduce waste material on high "buy:fly" ratio parts [16] has driven it to be a leading material in the aerospace industry's AM adoption. However, if the use of AM incurs higher inspection costs, then the cost advantage from material savings is lost. This makes titanium a good demonstration for why cost-effective NDE is a focus of industry.

2.2 Fabrication of Test Specimens

Two specimens of the nominal part design (Figure 1A), and one specimen of the defective part design (Figure 1B) were fabricated from Ti-6Al-4V powder via Electron Beam Melting (EBM) on an Arcam A2X machine. Figure 2 shows these three specimens in various states of release from their powder cakes after their 10 hour manufacturing session on single print bed. The 'cake' around

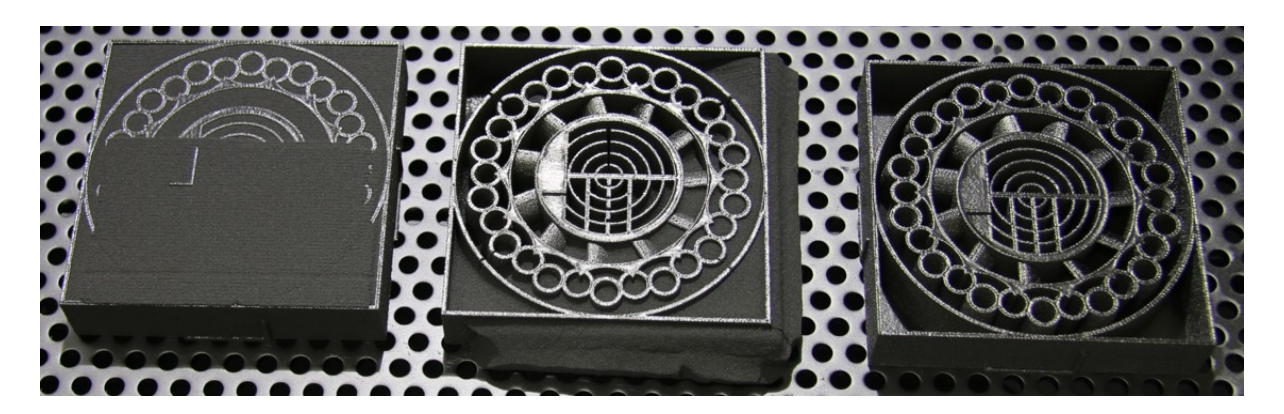


Figure 2. The three specimens being released from build cakes in a glove box. The flawed specimen is in the middle. The defect-free control specimens are on the left and right.

the three parts shown in Figure 2 required a total of twelve hours to remove. The two nominal part specimens (left and right) were used to establish the design's EMI "signature" baseline.

2.3 CT Scan Methodology and Parameters

The parts were intended to be scanned only through their 2 cm tall profiles, as if they were a 10% slice of a 20 cm long complex part, such as a heat exchanger. While this is how the parts were scanned with the 160 kV CT system, subsequent 220 kV CT scanning may have been performed face-on, as if through the long dimension of the heat exchanger. The higher power scan was desired by the NDE engineers tasked with this portion of the study to better resolve the internal voids. The scans were performed by a third-party scanning service, and rendered by that service, and the directions to not use the obvious and ideal direction to scan the part in may not have been followed.

2.4 EMI Analysis Methodology and Parameters

Each specimen was designed with L-shaped alignment rails on the sides (Figure 1A) to increase repeatability during the manual application of sensors. For this study, the sides facing away from the camera, at the top of the image in Figure 2, were used as the mounting location for each specimen. Before instrumentation, the mounting location was thoroughly cleaned of debris using a lint-free cloth, then rinsed with acetone to remove any remaining residue. After air drying, a PZT element was mounted to each specimen.

The PZT elements used in this study were diced from a PZT-5H wafer with nickel electrodes, purchased from Piezo Systems. In order to ensure consistent properties, and to minimize variations in EMI signature, all PZT elements used in this study were diced from a single PZT wafer. Each element had dimensions of $25.4 \times 12.7 \times 0.191$ mm. Copper tape with conductive adhesive was applied to the electrodes on the faces of each PZT element, which allowed electrical access to the underside and eliminated the need to solder directly onto the elements. After preparing the PZT elements, they were bonded to the test specimens using cyanoacrylate adhesive. Lead wires were then soldered to the copper tape before allowing the glue to cure for 24 hours at room temperature.

Prior to measurement, the specimen was suspended using monofilament line to imitate a free boundary condition. Each PZT-instrumented specimen was individually evaluated using a *Keysight E4990A Impedance Analyzer*. The impedance was measured using single-frequency sine-

wave excitation in a linearly spaced range from 1 kHz to 100 kHz in steps of 2 Hz. The step size was chosen to ensure sufficient density of measurement points to resolve any resonant peaks existing in the frequency range of interest based on a preliminary examination of the width of peaks. Above 100 kHz, variability in manufacture and instrumentation of the controls was expected to introduce too much noise to permit useful comparison of only two control specimens.

3. RESULTS

Following printing, two specimens (one of each part design) were CT imaged first using a *GE phoenix nanome*|x 180, then on a higher-powered *Nikon 225XTH* to assess scanner abilities, but without expending the cost to scan all three. Then all three specimens were instrumented with PZT elements, and their EMI signatures were measured using an impedance analyzer. Upon seeing the baseline specimens' signatures in strong disagreement, all three specimens were examined and determined to have inconsistency in the thickness of their bottom faces. This was addressed by machining away the bottom face entirely, in an attempt to increase consistency among the specimens. Then, the specimens were re-instrumented and their EMI signatures were re-measured.

3.1 Post-Manufacturing Machining

As discussed above, following both CT scans, the specimens were assessed using the EMI technique. However, when assessing the specimens after their first EMI characterization, it was seen that the specimens were of inconsistent thickness on their bottom face as measured at the four corners of the specimens. The height and depth of the corners, as indicated in Table 1, were measured. While the depth was found to be consistent across specimens, the height varied. The difference between the height and depth at each corner is represented in Table 1 as 'Thickness.' The cause of this defect is likely peeling of the parts off of the build plate, since the machine operator reported that the parts were not firmly attached to the build plate after fabrication. This peel up is likely due to the large flat bottom being printed onto the build plate. If the parts had been printed "upside down" instead, with the solid surface printed as the last layer, then the contraction of the build would have been "taken up" by residual powder between the print-bed and the first layer of the part, and the part would not have buckled up creating the inconsistent bottom surface.

Table 1. Comparison of design and specimens' corner thicknesses as fabricated, before machining, revealing an un-intended, yet fixable, manufacturing flaw.

er	Design	Control 1	Control 2	Defective	1
Corn	Thickness (mm)	Thickness (mm)	Thickness (mm)	Thickness (mm)	2
1		1.95	1.23	0.75	
2	2.00	1.20	0.31	1.23	Depth.
3	2.00	0.52	1.18	2.08	3
4		1.26	2.05	1.40	

After the specimens were EMI characterized, the PZT elements were removed by dissolving the adhesive with acetone. As shown in Figure 3, the specimens were machined to remove the bottom face, making the depth/height at all corners a consistent 18.4 mm and thereby increasing



Figure 3. Baseline specimen after bottom machining removal and post-second EMI testing. A PZT is seen attached on the top.

consistency among the specimens. Then, the same PZT elements were reapplied to their respective specimens for a second EMI characterization.

3.2 CT X-ray Scan Results

After fabrication, the defective specimen was CT scanned on a *GE phoenix nanome*|*x 180*, as shown in Figure 4A. An unflawed specimen was also scanned (not published here) and the results showed no voids present, but did show some remaining powder caked in and still stuck at the bottom of the part under solid features. After the first set of scans, the specimens were then scanned in a *Nikon 225XTH* system at 220 kV, as shown in Figure 4B. The figure shows approximately the same 'cuts' of the defective specimen at the same scale for both.

The field of view in Figure 4A is restricted compared to Figure 4B due to the 1,000 by 1,000 voxel system resolution being utilized to capture the smallest designed internal flaws the CT operator was told to look for. In practice, this size would be the allowed inclusion size specified by the designer of the part. The central image, A-A, shows some of the flaws: ten unfused squares of various sizes along the middle of the center 'spine' of the specimen. In these regions, trapped, unfused powder remains which has a lower net density, possibly 60 % [17] of the fused powder around it. The smallest flaws in the center of the specimen are only vaguely visible though in Figure 4A, and would warrant detailed re-scanning of that region to isolate. The B-B images shows the 'depth' of those unfused regions, as well a second set of 10 unfused flaws designed directly below the first, as seen in the Figure 1B, B-B cross sections. While this second set of flaws are only faintly seen in Figure 4A, they are clearer in Figure 4B. Finally, image C-C shows an additional designed-defect, an unfused region in the middle of a curved 'blade' feature of the part.

As shown in Figure 4B, this same defective specimen was next scanned on a higher power and resolution machine, a *Nikon 225XTH* system at 220 kV via a demonstration by Nikon. The internal flaws are more visible, and it can now be easily seen that the bottom of the part has a thickness variance as in images B-B and C-C, when looking at the middle verses the edges. Both CT systems allow for digital part importing and automatic comparison to the scanned specimen, which was not performed here, nor was automatic flaw detection software utilized to detect enclosed voids. In

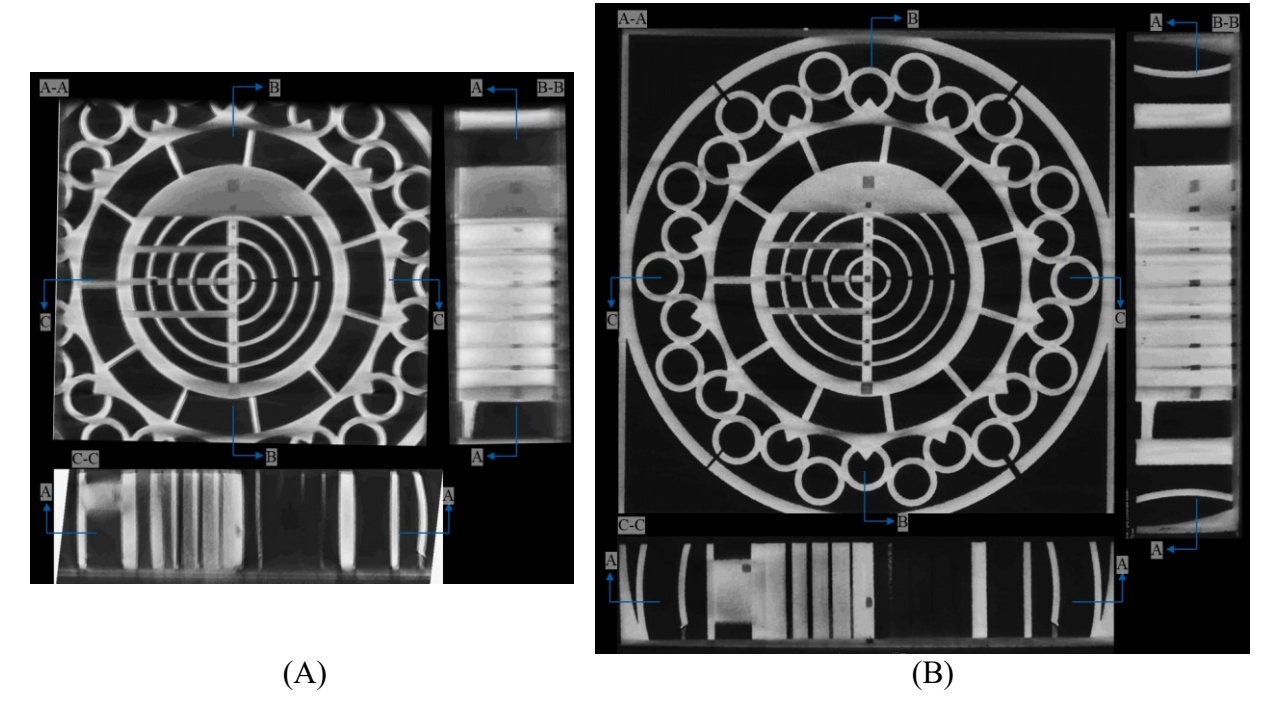


Figure 4. (A) 160kV CT scans of the defective specimen. (B) 220kV CT scan of the same part. Both have an upper, left image (A-A) which is a slice approximately mid-way through the specimen, as shown in the right (B-B) and bottom (C-C) images.

practice operators have apparently required a higher quantity of specimens of the same part design to efficiently utilize these features. This drove the analysis time to be roughly 8 hours.

3.3 Electromechanical Impedance Results

Shown in Figure 5 are impedance signatures taken of the control specimens both before and after machining, using the same measurement settings, the same PZT elements, and the same procedure described in section 2.4. It is important to point out that machining of the specimens completely alters their impedance signatures, since removing the bottom face fundamentally changes the structure of the specimens. However, assuming that the machining process removes a source of inconsistency between the control specimens, the post-machining signatures were expected to be in better agreement than the pre-machining signatures. This expectation was qualitatively borne out as seen in Figure 5. After machining, the number, position, and amplitude of the resonant peaks is much more consistent. Because the resonant peaks are so closely tied to the structural dynamics of the specimen, brief examination of the signatures suggests that the post-machining specimens are more similar than they were pre-machining. It is also worth noting that machining reduces the impedance signature on average, consistent with the idea that the bottom face adds to the specimen's overall stiffness.

Shown in Figure 6 are the two control and single defective specimen signatures both before and after machining. In this figure, the signatures have been slightly shifted vertically and horizontally to emphasize the difference in relative peak location. This is justified because shifts that shift the entire signature can be attributed to changes in the properties of the PZT element, such as those due to the temperature dependence of the also pyroelectric PZT [18], which was shown by Baptista

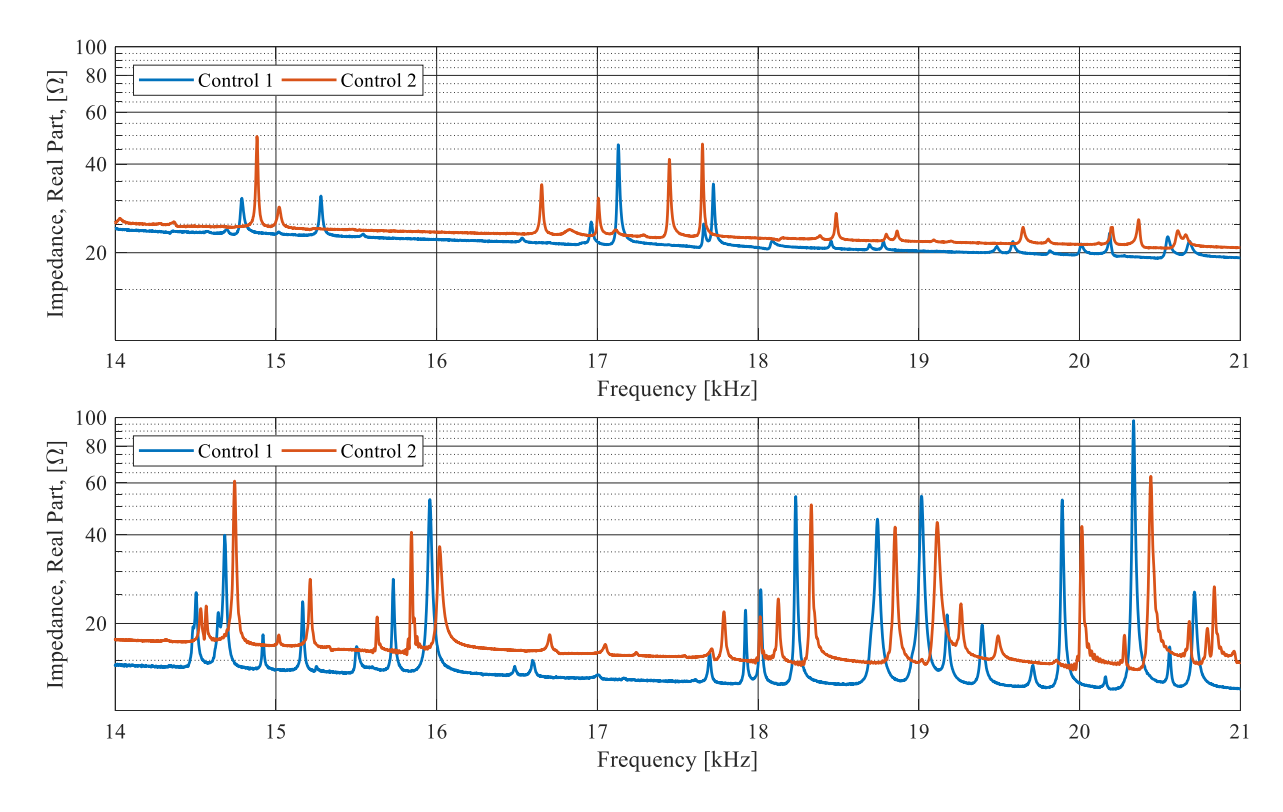


Figure 5. Impedance signatures for the pre-machining (top) and post-machining (bottom) control specimens. These data are not adjusted.

et al. to affect a roughly 8 Hz/°C shift in peaks. That would mean the approximately 100 Hz shift seen could be accounted for due to a 13 °C shift in temperature. It may be possible that differences are due to distributed, consistent changes throughout the specimen, such as a different average density or residual strain distribution due to build location on the plate. This alignment emphasizes that the peaks, which are more sensitive to local changes in the part, are very similar for the two control specimens post-machining. In contrast, there is not a frequency shift that brings the defective signature into a relative alignment with the control signatures. This is what one would expect, given a defective part that is so geometrically different than the controls.

3.3.1 Quantification of Damage

In order to quantify the post-machining agreement and put it in context, we can calculate the values of two damage-metrics: the widely-used root-mean-square deviation (RMSD) and a 'non-correlation' coefficient (r), which can each be calculated as shown below:

$$RMSD = \frac{1}{n} \sqrt{\sum \frac{(Z_D - Z_{BL})^2}{Z_{BL}^2}}$$
 (1)

$$r = 1 - \left| \frac{n \sum Z_D Z_{BL} - \sum Z_D \sum Z_{BL}}{\sqrt{[n \sum Z_D^2 - (\sum Z_D)^2][n \sum Z_{BL}^2 - (\sum Z_{BL})^2]}} \right|$$
(2)

In both definitions, Z_{BL} refers to the real component of the impedance signature being used as the 'baseline', Z_D refers to the real component of the signature corresponding to the potentially defective specimen, and n is the number of measurement points used for the comparison. Defined in this way, an increase in RMSD suggests increasing 'damage' as the responses diverge, while the non-correlation is inverse, decreasing with 'damage'. The RMSD measure can take any positive value. The non-correlation metric takes a value of zero when the signatures are identical and a value of one in the case of uncorrelated data. These metrics are calculated using the aligned data sets (Figure 6), between the two control specimens and between 'Control 1' and the defective specimen over the 14-21 kHz range, as shown in **Error! Reference source not found.**. The metrics calculated between the two controls have lower values than those between Control 1 and the defective specimen, as was expected based on the appearance of Figure 6. However, these plots do not convey the very large amount of damage present in the defective specimen.

Table 2. Damage metrics calculated over the 14-21 kHz range for the lower plot in Figure 6.

Damage Metric	Control 2 to Control 1	Defective to Control 1		
RMSD	14.5	15.9		
Non-correlation	0.46	0.90		

In summary, this testing illustrates that the impedance-based technique can produce signatures that qualitatively differentiate between specimens based on a collection of various defect types. In

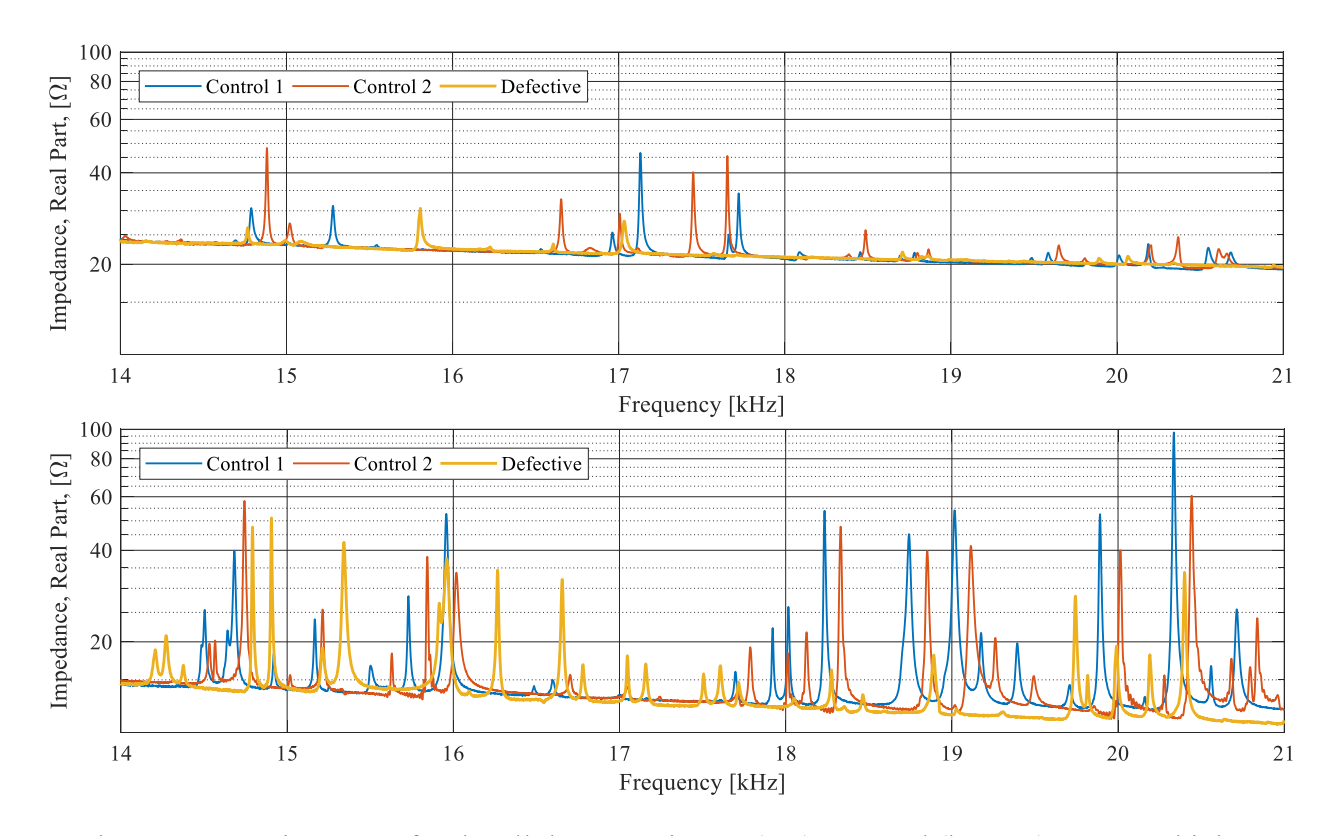


Figure 6. EMI signatures for the all three specimens (top) pre- and (bottom) post-machining. Signatures are aligned vertically in plots to emphasize difference in peak locations between specimens. In the bottom plot, the 'Control 2' signature is also shifted left by 100 Hz.

particular, it illustrates that bringing two specimens into closer geometrical agreement through machining away mm-level differences vastly improves the qualitative agreement between their impedance signatures.

3.4 Cost analysis

The cost of implementing AM in a production environment should consists of both the manufacturing cost and the cost of specimen inspection. Traditional subtractive manufacturing has a simpler quality control environment, in part due to its relative maturity, more structured process, and reduced set of production variables. These factors significantly reduce the requirements for post-production screening and testing compared to those for AM. Therefore, it is important to attempt to quantify the costs involved in NDE for AM, even at the very early stages.

Compiled in Table 3 is a breakdown of the NDE costs for four implementations of NDE 1) inhouse CT scanning of specimens, 2) use of a CT scanning service bureau, 3) in-house use of the EMI method, and 4) in-house use of an improved EMI method that reduces instrumentation time. The analysis to arrive at this table follows in respective sections.

Table 3. Cost comparison of CT and EMI methods to test n th specimen in a run of specimens at
current costs, and improved EMI method rates.

NDE Method	Capital Equip. (\$)	•	Scan-cost per Hour (\$)			Materials (\$)	Shipping (\$)	Sum per Specimen (\$)
1) CT bought	600,000	25	240	2	1,000	-	-	1,480
2) CT service	-	-	450	2	1,000	-	400	2,300
3) EMI, now	21,846	12.5	18	1	300	6	-	324
4) EMI, future	22,846	75	3	1	100	-	-	103

3.4.1 Analysis of Manufacturing Cost

Each of the three specimens required roughly \$160 of non-reusable powder titanium, \$600 of labor to remove the powder cake, and can be credited with a quarter of the 10 hour print on the *Arcam A2X* machine (an approximately \$1,500,000 capital asset [19], not including installation and support equipment costs). With this capital asset depreciated over five years of 4,000 hours of use each (16 hours per work day, as it has been commonly run), the machine 'costs' \$75/hour. This leads to each specimen costing \$188 in machine time. After including the cost of labor to de-cake, this means the specimens cost at least \$947 each to produce.

3.4.2 Estimating the Cost of CT Scanning

As shown in the first row of Table 3, the 220 kV CT system costs approximately \$600,000. Assuming this capital asset is depreciated over five years of 2,000 hours each (the machine is operated when an operator can be present), then it would have a pro-rated capital cost of \$60/hr. Unfortunately, these machines are often utilized at a lower duty rate in house, closer to quarter time. The two hours of scanning required per specimen have a 'machine cost' of about \$480/specimen when accounting for the asset's duty cycle. This also implies only one specimen is scanned per day. On top of this, CT scanning in-house of these specimens merely as part of a study has required roughly \$1,000 in technician and engineer analysis, increasing expected per-specimen

CT scanning cost to \$1,480. In other cases, anecdotally, parts and assemblies of this size have had increased analysis requirements driving costs to 5x or 10x this amount.

If a manufacturing organization does not have the volume of CT scanning needs to justify such a capital outlay, then external vendors may be used for scanning. This though, requires additional shipping, data transfer and often a higher per-hour scan cost. As shown in the second row of Table 3, in this instance the cost increased to \$2,300/per specimen. The parts in this work were hand delivered to the site of scanning, which cost significant employee time, and data transfer from the vendor required a dedicated hard drive. Despite this increased cost, use of a service bureau does not commit an organization to invest in a large capital asset, and may enable access to the leading edge of CT technology.

3.4.3 Estimating the Cost of EMI Signature Characterization

Performing EMI signature characterization requires an impedance measurement system. As shown in the third row of Table 3, the *Keysight E4990A* used in this study is quoted for sale at \$21,846 [20]. NDE via EMI required about 90 minutes per scan, though this time could be significantly reduced if the range of interrogated frequencies were reduced through preliminary evaluation. For an even comparison to the in-house CT scanner, this comparison at first assumed the more expensive use-case where specimens are not scanned at more than the same rate of one per day. Even then, spreading the capital asset costs across one part per working day for the same five years leads to the comparatively low cost of \$17.50/per specimen. With the lower dimensionality and complexity of the EMI signature, it is anticipated that the analysis engineer's time can be greatly reduced, and the technician work may also be reduced in time and skill compared to what is required for CT imaging. In this case, much of the remaining time is spent applying and removing the glued-on \$6 PZT element. With these assumptions, the cost of labor is reduced to roughly \$300 per specimen, and total cost (asset, material and labor) to \$324 per specimen as shown in Table 3.

An estimate of the future cost of EMI is shown in the last row of Table 3. As the main cost is primarily the 'touch time' required to apply and remove the PZT, alternate means of attaching the PZT would significantly reduce cost. Preliminary investigations into the use an instrumented clamp for impedance-based EMI have been conducted at Virginia Tech [14]. In the final row of Table 3, the operating costs for such a 'clamp-on' system are estimated. Such a system would increase the capital expense, eliminate the per-part material costs, and reduce the labor per scan by two thirds. This would reduce testing expense to around \$100 per specimen.

3.4.4 Cost/Effectiveness comparison between techniques

In a manufacturing environment, both methods require capital equipment and technician time. These costs were introduced in in Table 3, proportioned per specimen, and discussed in their sections. A large part of the cost difference is the capital expense: the *Keysight E4990A* is roughly 4% of the capital cost of a *Nikon 225XTH* CT scanner. Surprisingly though, the comparison in labor between the methods is even starker. The estimated labor difference is attributed to the huge reduction in data collected and analysis time spent. If the qualitative agreement observed in Figure 6 can be captured in a repeatable and quantitative way as attempted in Table 2, this analysis shows the potential for large reductions in cost.

Though this study does not show the sensitivity of the EMI method, it does demonstrate the current difficulty and expense involved in evaluating AM specimens. At least for large amounts of damage, the EMI method may answer screening needs for \$324 instead of \$1,480. With reduced labor costs, the EMI method's cost could be reduced to less than one tenth the cost of CT imaging.

4. CONCLUSIONS

Both CT scanning and EMI methods used were able to detect the presence of flaws. Though CT imaging provides detail on the size and location of flaws, there are production applications where great value is gained by simply screening their presence [1]. These two methods should likely be paired to maintain a healthy production of parts. In the same way that the medical community uses a thermometer to screen for illness, while a throat culture is used to diagnosis the infection for proper treatment, EMI may be an excellent screener to approve parts for use, while follow-up CT scans can be performed on AM parts with detected flaws. This is how the significantly lower estimated cost of the EMI method could enable a lower net cost for implementing AM in a production environment.

4.1 Remaining Technical Hurdles for EMI

In order to push the EMI evaluation technique towards to a COTs technique for industry adoption, three main areas of research need to be addressed: means of sensor application, quantification of lower detection limits, and automation of the analysis carried out on the observed signatures.

Application of the PZT sensor/actuator in this work was done manually and with the aid of alignment features built into the specimens. In order to encourage wider adoption, a simplified method of application should be investigated. This may take the form of automated bonding, embedding of PZT within the part, or 'clamp-on' attachment options. And it may be that different options are suited to different tasks: a permanently bonded sensor may increase instrumentation time, but allow for monitoring over the life of the part. But whatever the means, accurate and repeated location of the PZT element is essential for establishing a consistent basis for comparison of impedance signatures.

Additionally, the characterization of discrepancies between the baseline signature and an individual specimen's impedance signature needs to be further quantified. Widely used metrics such as root-mean-square deviation or the 'non-correlation' coefficient can provide a measure of the severity of damage in a part, but they are not designed with an understanding of the physics of the problem. Metrics that capture the shifting of resonant peaks and differentiate global shifts from local changes would give more insight into the condition of specimens. Moreover, screening of PZT wafers and temperature sensing at the time of measurement could better account for PZT wafers variability and pyroelectricity [18].

Finally further testing to identify minimum detectable flaw size is required. This work has shown that a collection of flaws can be very clearly detected, but did not isolate if any single flaw was or was not detectable, due to the large number of samples which will be required for that study.

4.2 Acknowledgements

The authors would like to thank the reviewers of this paper for their time. They would also like to thank Ian Day for advice on EBM fabrication limitations, Dr. Thomas Chung for advice on and sourcing of CT scans, and Louis Tiger and Nathan Reynolds for coordination of this collaborative research between Northrop Grumman Corporation and Virginia Polytechnic Institute and State University. The authors would also like to recognize the support of the John R. Jones III faculty fellowship. Portions of this research were supported by the National Science Foundation (NSF) under Grant No. 1635356. Any opinions, findings, and conclusions or recommendations expressed in this material are those of the author(s) and do not necessarily reflect the views of the NSF.

5. REFERENCES

- [1] Hrabe, Nikolas, N. Barbosa and S. Daniewicz. "Findings from the NIST/ASTM Workshop on Mechanical Behavior of Additive Manufacturing Components." NIST Advanced Manufacturing Series (2016).
- [2] Bergmann, Ralf B., Florian T. Bessler and Walter Bauer. "Non-Destructive Testing in the Automotive Supply Industry Requirements, Trends and Examples Using X-ray CT." Proceedings of the ECNDT 2006 Conference. 2006.
- [3] Roth, Don J. "Industrial X-ray Volumetric Computed Tomography." Materials Evaluation 74.7 (2016): 974-983.
- [4] Kenderian, S., et al. "A general overview of some Nondestructive Evaluation (NDE) techniques for materials characterization." Proceedings of SPIE. 2009.
- [5] Feser, M, et al. "Sub-micron resolution CT for failure analysis and process development." Measurement Science and Technology 19.9 (2008).
- [6] Fritzen, C. "Vibration-Based Techniques for Structural Health Monitoring." Structural Health Monitoring. ISTE, 2006. 45-52.
- [7] Crawley, Edward F. and Javier De Luis. "Use of piezoelectric actuators as elements of intelligent structures." AIAA Journal 25.10 (1987): 1373-1385.
- [8] Liang, C., F. P. Sun and C. A. Rogers. "Coupled Electro-Mechanical Analysis of Adaptive Material Systems-Determination of the Actuator Power Consumption and System Energy Transfer." Journal of Intelligent Material Systems and Structures 8.4 (1997): 335-343.
- [9] Peairs, Daniel M., Pablo A. Tarazaga and Daniel J. Inman. "Frequency Range Selection for Impedance-Based Structural Health Monitoring." Journal of Vibration and Acoustics 129.6 (2007): 701-709.
- [10] Naidu, A S K, S Bhalla and C K Soh. "Incipient damage localization with smart piezoelectric transducers using high-frequency actuation." Proceedings of SPIE. 2002.
- [11] Albakri, Mohammad I, et al. "Impedance-based non-destructive evaluation of additively manufactured parts." Rapid Prototyping Journal 23.3 (2017): 589-601.

- [12] Sturm, Logan, et al. "In-Situ Detection of Build Defects in Additive Manufacturing via Impedance-Based Monitoring." 27th Annual International Solid Freeform Fabrication Symposium An Additive Manufacturing Conference. 2016.
- [13] Tenney, Charles, et al. "Internal Porosity Detection In Additively Manufactured Parts Via Electromechanical Impedance Measurements." Conference on Smart Materials, Adaptive Structures and Intelligent Systems. Snowbird, UT: ASME, 2017. SMASIS2017-3856.
- [14] Tenney, Charles, Albakri, Mohammad I, Williams, Christopher B. and Tarazaga, Pablo, A.. "NDE of Additively Manufactured Parts via Directly Bonded and Mechanically Attached Electromechanical Impedance Sensors." (under review).
- [15] Peairs, Daniel M., Gyuhae Park and Daniel J. Inman. "Improving Accessibility of the Impedance-Based Structural Health Monitoring Method." Journal of Intelligent Material Systems and Structures 15.2 (2004): 129-139.
- [16] Allen, Jeff. "An Investigation into the Comparative Costs of Additive Manufacture vs. Machine from Solid for Aero Engine Parts." Cost Effective Manufacture via Net-Shape Processing. Neuilly-sur-Seine, France, 2006. 17-1 to 17-10. 2018.
- [17] Zielinski, Jonas, et al. "Influence of Powder Bed Characteristics on Material Quality in Additive Manufacturing." BHM Berg- und Hüttenmännische Monatshefte 162.5 (2017): 192-198. https://doi.org/10.1007/s00501-017-0592-9>.
- [18] Baptista, Fabricio G, et al. "An Experimental Study on the Effect of Temperature on Piezoelectric Sensors for Impedance-Based Structural Health Monitoring." Sensors 14 (2014): 1208-1227.
- [19] Arcam. "Arcam Annual Report 2016." Annual Financial Report. 2016. PDF. 22 1 2018.
- [20] Keysight. How to Buy or Rent: E4990A Impedance Analyzer, 16 January 2018. "https://www.keysight.com/en/pd-2405177-pn-E4990A/impedance-analyzer-20-hz-to-10-20-30-50-120-mhz?pm=HB&nid=-33831.1089074&cc=US&lc=eng>"https://www.keysight.com/en/pd-2405177-pn-E4990A/impedance-analyzer-20-hz-to-10-20-30-50-120-mhz?pm=HB&nid=-33831.1089074&cc=US&lc=eng>"https://www.keysight.com/en/pd-2405177-pn-E4990A/impedance-analyzer-20-hz-to-10-20-30-50-120-mhz?pm=HB&nid=-33831.1089074&cc=US&lc=eng>"https://www.keysight.com/en/pd-2405177-pn-E4990A/impedance-analyzer-20-hz-to-10-20-30-50-120-mhz?pm=HB&nid=-33831.1089074&cc=US&lc=eng>"https://www.keysight.com/en/pd-2405177-pn-E4990A/impedance-analyzer-20-hz-to-10-20-30-50-120-mhz?pm=HB&nid=-33831.1089074&cc=US&lc=eng>"https://www.keysight.com/en/pd-2405177-pn-E4990A/impedance-analyzer-20-hz-to-10-20-30-50-120-mhz?pm=HB&nid=-33831.1089074&cc=US&lc=eng>"https://www.keysight.com/en/pd-2405177-pn-E4990A/impedance-analyzer-20-hz-to-10-20-30-50-120-mhz?pm=HB&nid=-33831.1089074&cc=US&lc=eng>"https://www.keysight.com/en/pd-2405177-pn-E4990A/impedance-analyzer-20-hz-to-10-20-30-50-120-mhz-20-30-50-120-mhz-20-30-50-120-mhz-20-30-50-120-mhz-20-30-50-120-mhz-20-30-50-120-mhz-20-30-120-mhz-20
- [21] Muller, P, et al. "A study on evaluation strategies in dimensional X-ray computed tomography by estimation of measurement uncertainties." International Journal of Metrology and Quality Engineering 3.2 (2012): 107-115.
- [22] Kruth, J.P., et al. "Computed tomography for dimensional metrology." CIRP Annals Manufacturing Technology 60.2 (2011): 821-842.